RESEARCH ARTICLE | FEBRUARY 17 2023

Multi-peak emission of In_2O_3 induced by oxygen vacancy aggregation

Yin-Hui Peng; Chang-Chun He; Yu-Jun Zhao; ... et. al

Journal of Applied Physics 133, 075702 (2023)
https://doi.org/10.1063/5.0135162

Journal of Applied Physics ARTICLE scitation.org/journal/jap

Multi-peak emission of In_2O_3 induced by oxygen vacancy aggregation

Cite as: J. Appl. Phys. **133**, 075702 (2023); doi: 10.1063/5.0135162
Submitted: 5 December 2022 · Accepted: 2 February 2023 ·
Published Online: 17 February 2023

Yin-Hui Peng, Chang-Chun He, Yu-Jun Zhao, and Xiao-Bao Yang[a)]

AFFILIATIONS

School of Physics and Optoelectronics, South China University of Technology, Guangzhou 510640, China

[a)]**Author to whom correspondence should be addressed:** scxbyang@scut.edu.cn

ABSTRACT

Oxygen vacancy is crucial to the optical properties in In_2O_3, however, the single oxygen vacancy model fails to explain the observed multi-peak emission in the experiment. Herein, we have theoretically investigated the diversity of oxygen vacancy distribution, revealing the relationship between the defect configurations and the optical properties. Combining the first-principles calculations and bayesian regularized artificial neural networks, we demonstrate that the structural stability can be remarkably enhanced by multi-oxygen vacancy aggregation, which will evolve with the defect concentration and temperature. Notably, our results indicate that the single oxygen vacancy will induce the emission peaks centered at 1.35 eV, while multi-peak emission near 2.35 eV will be attributed to the distribution of aggregated double oxygen vacancies. Our findings provide a comprehensive understanding of multi-peak emission observed in In_2O_3, and the rules of the vacancy distribution may be extended for other metal oxides to modulate the optical properties in practice.

I. INTRODUCTION

Due to excellent photoelectronic properties, wide bandgap oxide semiconductors have been widely applied in flat-panel displays, solar cells, emerging flexible, and transparent electronics.[1–3] As an *n*-type semiconductor with high conductivity and good optical transparency, indium oxide (In_2O_3) has attracted extensive attention.[4] It has long been suspected that the oxygen vacancies are the origin of *n*-type conductivity in In_2O_3 because the oxygen partial pressure during growth or post-growth processing can affect the optical properties of In_2O_3.[5,6] In_2O_3 films have exhibited the optical bandgap of 3.62 eV and optical transmittance of 87% at an oxygen partial pressure of 2×10^{-3} mbar.[7] With the increasing oxygen partial pressure, the optical bandgap of the In_2O_3 thin film was also observed to increase gradually.[8] Also, oxygen partial pressure percentage would induce the morphology difference of In_2O_3 by modulating the spatial distribution of In and O atoms, further affecting the defect concentration, electron density, and Fermi level position.[6]

In the experiment, the synthesis temperature has played a significant role in the photoluminescence (PL) peak of In_2O_3. There is emission at 475 nm in the PL spectra of high-density and well-aligned In_2O_3 nanotubes synthesized at lower temperatures, indicating a deep defect level introduced by oxygen vacancy (V_O).[9] The blue emission peaks at 420 and 470 nm have been observed in the thermally oxidizing indium nanohillock at 500°C, and the high oxygen vacancies density has been detected in these In_2O_3 nanostructures.[10] For the In_2O_3 nanowires grown in the temperature of 1050°C, there are three deep defect level emission peaks in PL spectra, corresponding to the visible region centered at 423, 436, and 487 nm.[11] In the recent study, three main PL peaks, including 485, 505, and 795 nm, have been observed in the In_2O_3 thin layers annealed at 250 and 450 °C during 1 and 2 h.[12] Therefore, the multi-peak emission in the spectra might be attributed to the complex distributions of V_O, which will evolve as a function of synthesis temperature.

Theoretically, researchers have believed that the treatments of the first-principles calculations should be most important to the effect of V_O on optical properties, employing various methods such as the local density approximation (LDA), LDA+U, generalized gradient approximations (GGAs), GGA+U, and Heyd–Scuseria–Ernzerhof (HSE).[13–17] Based on the calculated by HSE06 with higher accuracy, the defect energy level induced by single V_O is about 2.25 eV above the valence band maximum (VBM).[15] Furthermore, when the Hartree–Fock mixing parameter is 0.28, the single V_O structure only gives rise to one emission peak at 2.3 eV.[17] In most theoretical studies, a supercell with 80 atoms is adopted to

model In_2O_3 with single oxygen vacancy because this system has been characterized by a large 1% O-deficient nonstoichiometry.[18–21] However, regardless of the change in calculation methods, the single vacancy model can only induce one peak emission of In_2O_3. Recent studies have shown that the distribution of oxygen vacancies in TiO_2, SiO_2, and HfO_2 can affect the electronic structure properties, while our recent progress has shown that the configuration with double vacancies will be more stable than that with single vacancy in In_2O_3.[22–25] Thus, the effect of V_O distribution should be considered, which will provide a reasonable explanation of the multi-peak emission.

In this paper, we have systematically studied the structural stability of In_2O_3 with various distributions of oxygen vacancies based on the first-principles calculations, employing the HSE06 hybrid functional to obtain accurate optical properties. To give a good estimation of structural stability, we use bayesian regularized artificial neural networks (BRANNs) to get the relationship between oxygen vacancy distance and defect formation energy from the first-principles calculations.[26] The stable structures are determined based on the formation of energies, and the evolution of vacancy distribution is demonstrated as a function of temperature by considering the contribution of configuration entropy. In optical properties, we have confirmed the emission centers for single and double oxygen vacancies based on the simulation of excited states, which indicates that the multi-peak emission are attributed to multi-oxygen vacancy aggregation.

II. METHODS

The first-principles calculations based on density-functional theory were performed with Vienna *Ab initio* Simulation Package (VASP).[27,28] The Perdew–Burke–Ernzerhof (PBE) generalized gradient approximation was used to describe the exchange–correlation interaction.[29,30] The Brillouin zone was sampled with allowed spacing between points in 0.3 $Å^{-1}$. Cutoff energy of 520 eV and residual atomic forces criteria of 0.02 eV/Åwere selected in all simulations. To avoid the underestimation of bandgap for traditional metal oxide semiconductors, the HSE06 hybrid functional was adopted to improve the description of band structure and density of state (DOS).[31] The ΔSCF method was employed to simulate excited states.[32–34] In this way, we will construct the different electronic configurations by a set of orbitals occupation. Based on the electronic ground-state configuration with a set of occupied orbitals, an excited state of In_2O_3 can be obtained by emptying one of the occupied orbitals and filling one of the unoccupied orbitals.

It is known that the V_O concentration will reach 1% in the experiments under the O-poor condition.[18–21] The supercells of $80 \times n$ ($n = 1 \sim 7$) atoms were generated with the Hermite normal form matrices, and n oxygen vacancies were introduced in the supercell with $80 \times n$ atoms, respectively.[35,36] Based on the Structures of Alloy Generation and Recognition (SAGAR),[36] the structural multiplicity will be obtained. With such concentrations, the V_O is generally in a neutral charge state under the charge neutrality restriction.[25] Therefore, we give priority to the neutral V_O as the main defect. The formation energy of neutral defect α can be calculated as follows:[37]

$$\Delta H_D^{(\alpha)} = E(\alpha) - E(0) + \sum_\alpha n_\alpha(\Delta\mu_\alpha + \mu_\alpha), \quad (1)$$

where $E(\alpha)$ is the total energy of the supercell containing the defect α; $E(0)$ is the total energy of perfect supercell; n_α is the number of atoms corresponding to defect α; a positive or negative value of n_α indicates the atoms are removed or added. $\Delta\mu_\alpha$ is the chemical potentials of defect α; μ_α is total energy of the most stable phase corresponding to defect α.

The average formation energy with the different number of oxygen vacancies (ΔE_{V_O}) is used to describe the structural stability of supercells, and the formula is given by

$$\Delta E_{V_O} = \Delta H_D^{(\alpha)}/n_\alpha. \quad (2)$$

To consider the temperature effect on structural stability, the Gibbs free energy F for a solid system ignoring volume changes is calculated by the following equation:[38] $F = kT \ln Z$. The partition function Z is expressed as $Z = \sum_i \omega_i e^{-\beta E_i}$, where ω is the structural multiplicity for the system. The occurrence probability of structure p_i with defect α can be shown as

$$p_i = \omega_i e^{-\beta \Delta E_{V_O}^i}/Z, \quad (3)$$

where $\Delta E_{V_O}^i$ is the average formation energy of structure p_i.

The concentration of oxygen vacancies in In_2O_3 has been reported to affect the optical properties,[21] so we first exclude the contribution of defect concentration during the calculation process. We construct the structures with the same concentration and focus on the defect concentration (c_d) with $c_d = 1/48$, which is generally adopted by previous studies.[13–17] In the supercell of proper size, the V_O interaction from the periodic images is small enough to be neglected, and those perfect supercells are shown in supplementary material, Fig. S1.

III. RESULTS AND DISCUSSION

A. The stable distribution of oxygen vacancies

According to the enumeration with structural recognition, we obtain the formation energies of all structures with single vacancy and double vacancies. When the supercell reaches 240 atoms, there are 40 621 nonequivalent structures with triple vacancies. As the supercell grows larger, there are more than one hundred million structures, and the computational cost becomes over expensive. Thus, the BRANNs are employed to predict the relationship between oxygen vacancy distance and ΔE_{V_O}.[26] Our dataset contains all structures for 40 and 80 atoms with triple oxygen vacancies, and 150 structures are selected in the supercells with 120, 160, 200, and 240 atoms, respectively. We obtain the first nearest neighbor distances between the V_O in supercells with triple oxygen vacancies and the 150 structures are selected uniformly for each supercell according to the average distance. The relationship between the average distances of triple oxygen vacancies and the formation energy is shown in supplementary material, Fig. S2. We observe that with the increase of the average distance, ΔE_{V_O} first increases,

then decreases, and, finally, converges. The structures are more stable when the oxygen vacancies overall tend to be aggregated. We describe the configurations by the distances among all oxygen defects under the periodic boundary conditions, as shown in Fig. 1(a). Based on BRANNs, the error is smaller and the correlation coefficient R^2 of the model is 0.945, as shown in Fig. 1(b).

Figure 1(c) shows the relationship between supercell size and average defect formation energy under O-poor condition ($\mu_O = -2.74$ eV and $\mu_{In} = 0$ eV) . There is only one type of O site according to the Wyckoff position in the In_2O_3 bixbyite structure. The structure of 80 atoms with single V_O has only one configuration, and ΔE_{V_O} is 0.745 eV. For double oxygen vacancies in the supercell of 160 atoms, we calculated all the configurations by DFT, and evaluated the ΔE_{V_O} by BRANNs for comparison. The most stable supercells predicted by model and DFT are the same configuration, and the lowest ΔE_{V_O} calculated by DFT is 0.527 eV. Thus, the model evaluation with BRANNs is found to be accurate and efficient. Similarly, we used the trained model to predict oxygen vacancy defects in supercells with $80 \times n$ ($n = 3-7$) atoms. Due to the large number of defect configurations in supercell sizes ranging from 320 to 480, the 100 000 defect configurations were randomly selected to predict ΔE_{V_O}. In addition, the ten of most stable structures under each type of supercell were confirmed by the DFT calculation, determining the most stable defect configurations in the corresponding supercells. The lowest ΔE_{V_O} decreases from 0.548 to 0.338 eV in supercell sizes ranging from 240 to 480. Interestingly, there is a magic structure with aggregated six-oxygen vacancy in the supercell of 480 atoms as shown in structure G of Fig. 2.

Figure 2 shows the distributions of oxygen vacancies for the stable configurations in supercells with $80 \times n$ ($n = 1-6$) atoms. In structure A, the introduction of single V_O gives rise to the repulsion of In atoms near V_O, shortening of bond length. The average distance among the In atoms increases by 0.15 Å, as shown in supplementary material, Fig. S3(a). For two stable double V_O configurations (B and C) in the supercell of 160 atoms, we employ In-2V_O to mark one In atom losing two oxygen atoms. There are two In-2V_O in structure B, and only one In-2V_O in structure C. Both In-2V_O in structure B and C move toward the center of double oxygen vacancies, while the other neighboring In atoms are repulsed. The distances between In–In bonds are given in supplementary material, Fig. S3, and we find that the repulsion for In–In bonds around double oxygen vacancies is stronger than those around single vacancy. With shortening, the distance between double oxygen vacancies, the stronger repulsive Coulomb forces of In–In bonds can strengthen In–O bonds near V_O, enhancing the structural stability. In the most stable structure D with triple oxygen vacancies, the aggregation structure is also energetically preferable. Furthermore, the stable structure of the triple vacancy can be considered the introduction of an additional oxygen vacancy around the In-2V_O. Interestingly, the structures D, E, F, and G contain 1, 1, 2, and 4 In-3V_O respectively. The lowest ΔE_{V_O} is the structure G with six-vacancy, and the distribution of V_O is an octahedron. There are four In-3V_O near the octahedron, and those are not on adjacent octahedral surfaces. Each additional V_O repels a set of In atoms, strengthening a set of In–O bonds around vacancies. However, when the seven vacancies are aggregated, the weakened repulsive force of In atoms around the vacancy can be obviously observed. The distances of In atoms in those structures are shown in supplementary material, Fig. S3. Thus, six vacancies will form a magic cluster of aggregated oxygen vacancies, and the structural stability is attributed to the repulsion between the In atoms near oxygen vacancies. The aggregation of oxygen vacancies can increase the number of strengthened In–O bonds, improving structural stability.

In order to determine the effect of aggregated V_O on structural stability from the perspective of electronic structure, we use crystal

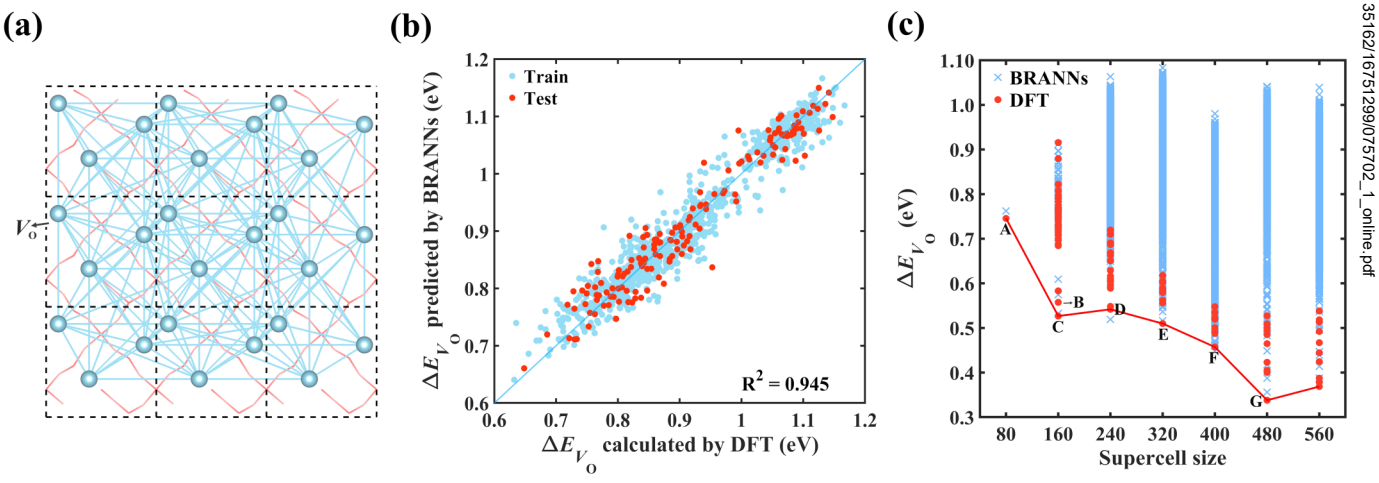

FIG. 1. (a) One wireframe graphic structure with the triple oxygen vacancies for In_2O_3. A black box represents one lattice period, and the blue ball shows the V_O. The blue line shows the distance between oxygen vacancies, while the red background box shows the line between the In and O atoms. (b) Comparison of ΔE_{V_O} predicted by the BRANNs and DFT. R^2 is the correlation coefficient. (c) ΔE_{V_O} varies with the supercell size under O-poor condition at 1/48 vacancy concentration. ΔE_{V_O} represented by letters corresponds to the structures in Fig. 2.

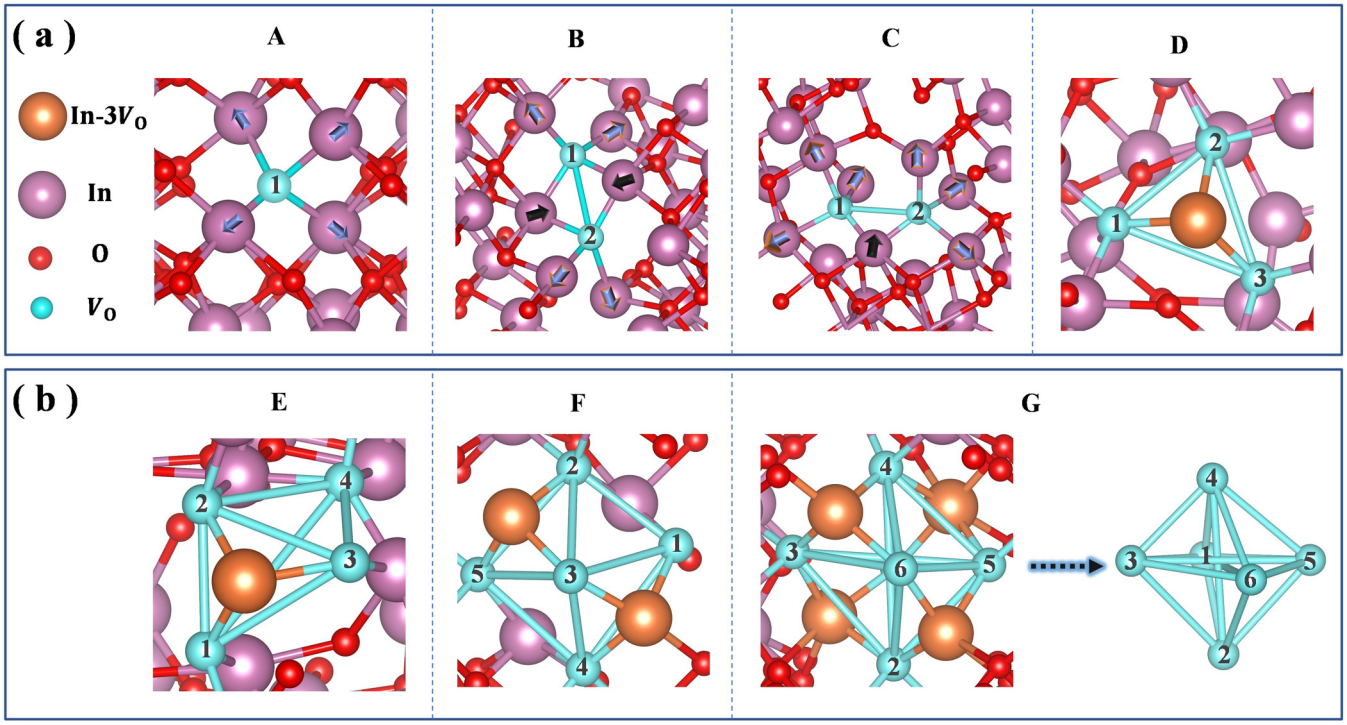

FIG. 2. Vacancy distribution of stable configurations at different supercell sizes. (a) 80, 160, 160, 240 atoms. (b) 320, 400, 480 atoms. In-3V_O represents the orange In atom losing three oxygen atoms. The arrows show the direction of movement for the In atoms after relaxation.

orbital Hamilton populations (COHP) to discuss bonding between atom pairs.[39,40] The positive value of –COHP indicates bonding states, whereas the negative value indicates antibonding states. As shown in Fig. 3(a), the –COHP shows that the In–O interactions are mainly bonding states in the defect-free In_2O_3. The In–O bonds form the antibonding states below the Fermi level in the structures with vacancy, whereas it can be attributed to the structural distortion caused by the introduction of V_O. Thus, the expelling O atoms immediately weaken In–O bonding states and are energetically unfavorable. Note that the In–O antibonding states

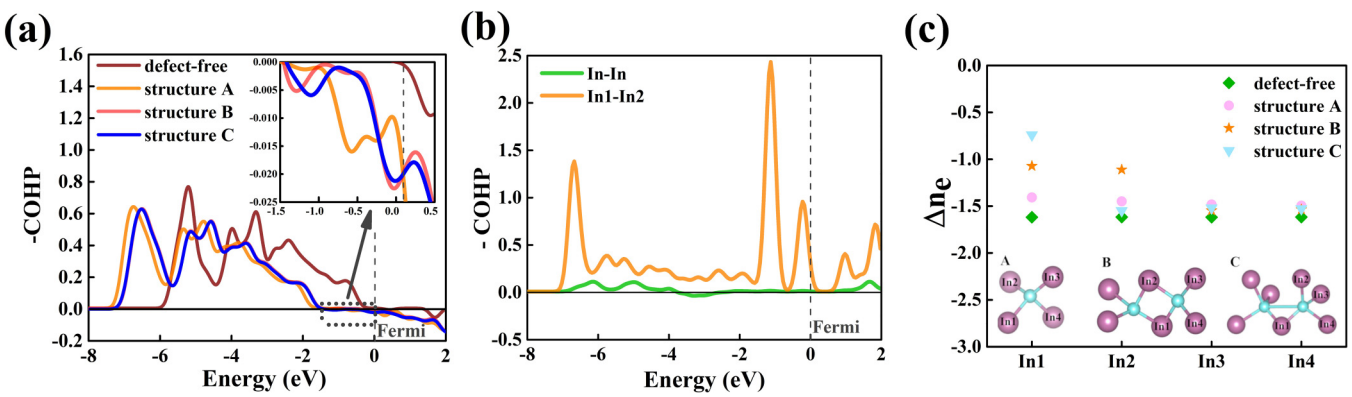

FIG. 3. (a) Negative crystal orbital Hamilton population of In–O bond in the structure of A, B, C, and defect-free. (b) Negative crystal orbital Hamilton population of average In–In bonds and single In1–In2 bond in structure B. (c) The Bader charges of In atoms around the oxygen vacancies in the structure of A, B, C, and defect-free. The negative value of Δn_e represents the number of electrons lost by one In atom.

for expelling two adjacent O atoms is weaker than expelling single O atom. On structural relaxation, the structures for aggregated oxygen vacancies are more stable. Furthermore, there is a pair of In–In bonds in structure B as shown in Fig. 3(b), which is consistent with the two In atoms moving towards each other. Compared with structure C, the pair of In–In bonds will enhance In–O antibonding, thus slightly reducing structural stability. Figure 3(c) shows that In atoms in structures B and C lose less charge than that in structure A, based on the charge transfer by the Bader analysis.[41] The In-2V_O of structure C has more charge than the In-2V_O of structure B with the absence of In–In bond. The number of paired electrons between the In and the O atoms around the double oxygen vacancies increases, strengthening the stability of the In–O bond.

B. The optical properties modulated by the distributions of double oxygen vacancies

Due to the diversity of experimental synthesis conditions, there may be a variety of defects in the preparation of In_2O_3. Based on the Boltzmann distribution, the vacancy concentration under thermodynamic equilibrium at growth temperature T_g is estimated as:[25] The oxygen vacancy concentration of single and double are 0.57%, 2.58%, respectively at $T_g = 1673$ K.[20] The In_2O_3 is characterized by a non-stoichiometric ratio of 1% O-deficient at this growth temperature T_g, indicating a mixed distribution of single and double vacancies with different probabilities. Therefore, we study the free energy variation of defect structure with the temperature by considering the configuration entropy attributed to structural multiplicity. The system with given concentration of vacancy is considered the canonical ensemble, and the number of possible configurations is estimated by combination. Taking the structure with six oxygen vacancies as an example, the structural multiplicity of single vacancy is represented by the number of combinations formed by six oxygen vacancies that are not close to each other. When facing the aggregated double oxygen vacancies, we regard the adjacent double oxygen vacancy as a local structure, and the three local structures are far away from each other. The structural multiplicity with aggregated double oxygen vacancies is given by the number of combinations, and changes with the defect concentration. Similarly, the combination of aggregated triple, four, five, and six oxygen vacancies are given correspondingly. For a given defect concentration and temperature, we estimate the probability of these V_O configurations according to the Eq. (3), as shown in Fig. 4(a). The probability for the structure with triple, four, and five oxygen vacancies are small enough to be neglected, and only the probability for structures with single, double, and six oxygen vacancies are shown in Fig. 4(a). When the V_O concentration is 1/100, the probability of structure with the six-vacancy aggregation is the highest at low temperatures. With the increase in temperature, the probability of the structure of a double vacancy configuration is obviously superior. However, when the V_O concentration is 1/200 and the experimental temperature exceeds 800 K, the defect configuration of single vacancy is obviously more likely to appear, rather than double vacancies. The detailed phase diagram as a function of defect concentration and temperature is given in Fig. 4(b). Considering the defect concentration from 0.1% to 1%, the six-vacancy aggregation will energetically preferable at low temperatures, which will evolve into double vacancies and, finally, single vacancy as the temperature increases. The critical temperature of the transition from aggregated six vacancies to aggregated double vacancies is almost the same, while the temperature of transition from double vacancies to single vacancy depends on the concentration dramatically. At the synthesis temperature (450−1050°C) of In_2O_3,[9–12] the phase diagram indicates that aggregated double oxygen vacancies will appear when the synthesis concentration of oxygen vacancies is higher than 1/150. Note that, In_2O_3 is characterized by a non-stoichiometric ratio of 1% O-deficient in experiments.[18–21] Therefore, double oxygen vacancies should be the majority of defects under common conditions.

Besides the structural stability, the optical properties will be dominated by the aggregation of multi-oxygen vacancy. The HSE06 was used to overcome the problem of underestimating the bandgap, and the electronic band in the reciprocal space is shown in supplementary material, Fig. S4. The calculated bandgap of In_2O_3 given by PBE is 0.90 eV, while the one by HSE06 is 2.57 eV, which is in good agreement with the previous result.[15]

In Fig. 4(c), we have shown the DOS of In_2O_3 with and without V_O, focusing on the variation with the distance of double oxygen vacancies. The O atoms are surrounded by four In nearest neighbors in In_2O_3, with four slightly different In–O bond lengths. The formation of V_O induces four In dangling bonds, which consist of a lower energy α_1 state in bandgap and three higher energy states in the conduction band. The α_1 state is located at 2.1 eV above the VBM in single V_O, whereas the double oxygen vacancies introduce two energy states in the bandgap, and the deeper state is marked as α_1' state. Interestingly, the α_1' state gradually moves toward the conduction band minimum (CBM) with the distance of the double oxygen vacancies increasing, while the α_1'' state first moves toward the CBM and then moves toward the VBM. Owing to the weakened interaction between the oxygen vacancies , the two energy states in the gap become almost degenerate, eventually forming a single energy state. As shown in Fig. S5 of the supplementary material, we have obtained structures A, C, and G with partial charge densities from defect states, corresponding to single-, double-, and six-vacancy, respectively. The charge distribution in the gap state is mainly localized around the defect. The variation of defect states induced by the spatial distribution of oxygen vacancies will effectively modulate the optical properties.

The multi-peak emission of In_2O_3 have been observed in the recent experiment, including 485, 505, and 795 nm.[12] In order to understand these emission centers caused by defect states, we employed ΔSCF method to simulate excited states, and focusing on the optical properties of single and double neutral oxygen vacancies based on the results discussed in Fig. 4(b).[32–34] The schematic diagram of electron-hole pairs induced by oxygen vacancies under external field excitation is shown in Fig. 4(d). When the electron of VBM is excited above the CBM, the system is in excited state. After lattice relaxation, the electron in the defect state falls back to the VBM accompanied by a luminescence process. In view of the higher thermal barrier induced by the instability of the single V_O, we predict a broad emission peak centered at 1.35 eV. In the structure of double oxygen vacancies, the emission peak centered at 2.35 eV is significantly higher than that of single V_O. Since the

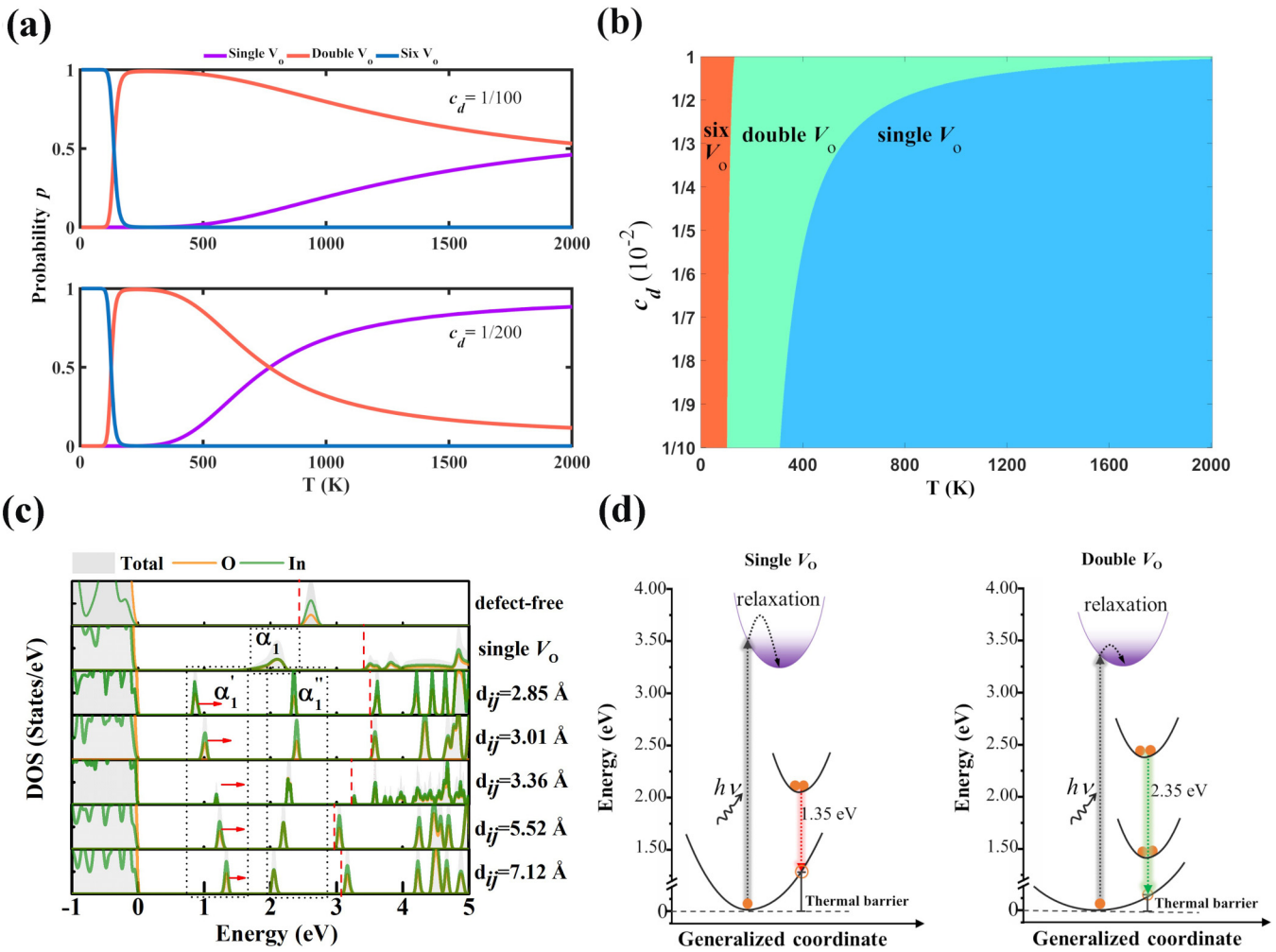

FIG. 4. (a) The probability of configurations with aggregated n ($n = 1, 2, 6$) oxygen vacancies under the Boltzmann distribution at defect concentration of 1/100 and 1/200. (b) The structural stability with n ($n = 1, 2, 6$) oxygen vacancies in In_2O_3 as a function of concentration c_d and temperature T. In a certain concentration and temperature, the structure for specific defect is dominant in the given area. (c) The total and atom-projected DOS for the defect-free, single V_O, and different double oxygen vacancies in In_2O_3. The zero position is VBM, and the red dashed lines represent the CBM. The α_1 state represents the defect state induced by the single V_O, while the α_1' and α_1'' states circled by the black dashed lines respectively refer to the deeper and shallower defect states induced by double oxygen vacancies. The d_{ij} is the relative position between the oxygen vacancies i and j. (d) Calculated configuration coordinate diagram of the optical transition for single oxygen vacancy (structure A) and double oxygen vacancies (structure C).

bandgap is slightly 0.1 eV lower than the experimental gap of 2.67 eV, we infer that the two calculated emission peaks, respectively, correspond to emission peaks near 795 and 505 nm. Note that the thermal barrier of double oxygen vacancies is significantly lower than that of the single V_O, which is in agreement with the experimental observation that the PL intensity near 795 nm is evidently weaker than the intensity near 505 nm.[12] As shown in Fig. 4(c), the position of the α_1'' state will change with the distance between the oxygen vacancies. The double oxygen vacancies with different distributions may lead to various emission peaks near 2.35 eV, corresponding to the multi-peak emission of In_2O_3. Thus, the peaks at 485 and 505 nm are attributed to double oxygen vacancies, rather than the single V_O.

IV. CONCLUSION

In summary, we have demonstrated that the aggregation of oxygen vacancies will be energetically preferable combining the BRANNs and the first-principles calculations. The aggregated six-oxygen vacancy is an octahedral defect, and the four In-3V_O are distributed on non-adjacent octahedral surfaces. The calculated free energy shows that the double oxygen vacancies are dominant at the

common condition due to the contribution of configuration entropy. In addition, the structural distortion induced by V_O will lead to charge redistribution, and form many localized defect states, resulting in the multi-peak emission in In_2O_3. The experimentally observed peaks at 485 and 505 nm are attributed to double oxygen vacancies, while the single vacancy mainly induces an emission peak at 795nm. Our calculation results fully illustrate that different oxygen vacancy distributions will affect the structural stabilities and optical properties, which is of great significance to the study of other non-stoichiometric oxides.

SUPPLEMENTARY MATERIAL

The supplementary material includes supercell structure corresponding to the 80, 160, 240, 320, 400, and 480 atoms (Fig. S1), ΔE_{V_O} varies with the average distances of triple oxygen vacancies under O-poor conditions (Fig. S2), the relative positions of In atoms before and after optimization of defect structures with oxygen vacancies (Fig. S3), the electronic band dispersion diagram for In_2O_3 calculated at the PBE and HSE06 level of the theory (Fig. S4), the partial charge densities from defect states of structures A, C, and G (Fig. S5).

ACKNOWLEDGMENTS

This work was supported by the National Key R&D Program of China (No. 2018YFB1502101), Guangdong Basic and Applied Basic Research Foundation (Grant Nos. 2021A1515010328 and 202201010090), and the National Natural Science Foundation of China (Grant No. 1207412).

AUTHOR DECLARATIONS

Conflict of Interest

The authors have no conflicts to disclose.

Authors Contribution

Y.-H.P. and C.-C.H. contributed equally to this work.

Yin-Hui Peng: Methodology (equal); Writing – original draft (equal). **Chang-Chun He:** Formal analysis (equal); Software (equal). **Yu-Jun Zhao:** Investigation (equal); Methodology (equal); Writing – original draft (equal). **Xiao-Bao Yang:** Supervision (equal); Writing – review & editing (equal).

DATA AVAILABILITY

The data that support the findings of this study are available from the corresponding author upon reasonable request.

REFERENCES

[1]M. Katayama, "TFT-LCD technology," Thin Solid Films **341**, 140–147 (1999).
[2]E. Fortunato, D. Ginley, H. Hosono, and D. C. Paine, "Transparent conducting oxides for photovoltaics," MRS Bull. **32**, 242–247 (2007).
[3]O. Bierwagen, "Indium oxide—A transparent, wide-band gap semiconductor for (opto)electronic applications," Semicond. Sci. Technol. **30**, 024001 (2015).
[4]J. Shi, J. Z. nad Lu Yang, M. Qu, D.-C. Qi, and K. H. L. Zhang, "Wide bandgap oxide semiconductors: From materials physics to optoelectronic devices," Adv. Mater. **33**, 2006230 (2021).
[5]O. Bierwagen and J. S. Speck, "High electron mobility In_2O_3(001) and (111) thin films with nondegenerate electron concentration," Appl. Phys. Lett. **97**, 072103 (2010).
[6]A. Chen, K. Zhu, H. Zhong, Q. Sha, and G. Ge, "A new investigation of oxygen flow influence on ito thin films by magnetron sputtering," Sol. Energy Mater. Sol. Cells **120**, 157–162 (2013).
[7]S. Kaleemullaa, A. S. Reddyc, S. Uthannab, and P. S. Reddy, "Physical properties of In_2O_3 thin films prepared at various oxygen partial pressures," J. Alloy. Compd. **479**, 589–593 (2009).
[8]A. V. M. Ali and D. Kekuda, "Thickness and oxygen partial pressure dependence on optical band gap of indium oxide by reactive evaporation method," IOP Conf. Ser.: Mater. Sci. Eng. **73**, 012027 (2015).
[9]X. ping Shen, H. jiang Liu, X. Fan, Y. Jiang, J. ming Hong, and Z. Xu, "Construction and photoluminescence of In_2O_3 nanotube array by CVD-template method," J. Cryst. Growth **276**, 471–477 (2005).
[10]H.-L. Wei, L. Zhang, Z.-L. Liu, and K.-L. Yao, "Fabrication and photoluminescence characteristics of In_2O_3 nanohillocks," Chin. Phys. B **20**, 118102 (2011).
[11]P. Wu, Q. Li, C.-X. Zhao, D.-L. Zhang, L. fei Chi, and T. Xiao, "Synthesis and photoluminescence property of indium oxide nanowires," Appl. Surf. Sci. **255**, 3201–3204 (2008).
[12]N. Beji, M. Reghima, M. Souli, and N. Kamoun Turki, "Effect of nitrogen annealing on the structural, optical and photoluminescence properties of In_2O_3 thin films," J. Alloy. Compd. **675**, 231–235 (2016).
[13]S. Lany and A. Zunger, "Dopability, intrinsic conductivity, and nonstoichiometry of transparent conducting oxides," Phys. Rev. Lett. **98**, 045501 (2007).
[14]P. Agoston, P. Erhart, A. Klein, and K. Albe, "Geometry, electronic structure and thermodynamic stability of intrinsic point defects in indium oxide," J. Phys.: Condens. Matter **21**, 455801 (2009).
[15]P. Ágoston, K. Albe, R. M. Nieminen, and M. J. Puska, "Intrinsic *n*-type behavior in transparent conducting oxides: A comparative hybrid-functional study of In_2O_3, SnO_2, and ZnO," Phys. Rev. Lett. **103**, 245501 (2009).
[16]S. Limpijumnong, P. Reunchan, A. Janotti, and C. G. Van de Walle, "Hydrogen doping in indium oxide: An *ab initio* study," Phys. Rev. B **80**, 193202 (2009).
[17]I. Chatratin, F. P. Sabino, P. Reunchan, S. Limpijumnong, J. B. Varley, C. G. Van de Walle, and A. Janotti, "Role of point defects in the electrical and optical properties of In_2O_3," Phys. Rev. Mater. **3**, 074604 (2019).
[18]J. H. W. De Wit, G. Van Unen, and M. Lahey, "Electron concentration and mobility in In_2O_3," J. Phys. Chem. Solids **38**, 819–824 (1977).
[19]J. H. W. De Wit, "The high temperature behavior of In_2O_3," J. Solid State Chem. **13**, 192–200 (1975).
[20]J. H. W. De Wit, "Structural aspects and defect chemistry in In_2O_3," J. Solid State Chem. **20**, 143–148 (1977).
[21]J.-Y. Gan, X.-H. Lu, J.-H. Wu, S.-L. Xie, T. Zhai, M.-H. Yu, Z.-S. Zhang, Y.-C. Mao, and Y.-X. Tong, "Oxygen vacancies promoting photoelectrochemical performance of In_2O_3 nanocubes," Sci. Rep. **3**, 1021 (2013).
[22]T. Li, F. Hong, K. Yang, B. Yue, N. Tamura, H. Wu, Z. Cheng, and C. Wang, "Metastable oxygen vacancy ordering state and improved memristive behavior in TiO_2 crystals," Sci. Bull. **65**, 631–639 (2020).
[23]M. C. Sahu, S. K. Mallik, S. Sahoo, S. K. Gupta, R. Ahuja, and S. Sahoo, "Effect of charge injection on the conducting filament of valence change anatase TiO_2 resistive random access memory device," J. Phys. Chem. Lett. **12**, 1876–1884 (2021).
[24]D. Z. Gao, J. Strand, M. S. Munde, and A. L. Shluger, "Mechanisms of oxygen vacancy aggregation in SiO_2 and HfO_2," Front. Phys. **7**, 43 (2019).
[25]L. Liu, C.-C. He, J. Zeng, Y.-H. Peng, W.-Y. Chen, Y.-J. Zhao, and X.-B. Yang, "Theoretical study of oxygen-vacancy distribution in In_2O_3," J. Phys. Chem. C **125**, 7077–7085 (2021).
[26]D. J. MacKay, "Bayesian neural networks and density networks," Nucl. Instrum. Methods Phys. Res., Sect. A **354**, 73–80 (1995).

[27]G. Kresse and J. Furthmüller, "Efficient iterative schemes for ab initio total-energy calculations using a plane-wave basis set," Phys. Rev. B **54**, 11169–11186 (1996).
[28]G. Kresse and D. Joubert, "From ultrasoft pseudopotentials to the projector augmented-wave method," Phys. Rev. B **59**, 1758–1775 (1999).
[29]P. E. Blöchl, "Projector augmented-wave method," Phys. Rev. B **50**, 17953–17979 (1994).
[30]J. P. Perdew, K. Burke, and M. Ernzerhof, "Generalized gradient approximation made simple," Phys. Rev. Lett. **77**, 3865–3868 (1996).
[31]J. Heyd, G. E. Scuseria, and M. Ernzerhof, "Erratum: 'Hybrid functionals based on a screened coulomb potential,'" J. Chem. Phys. **124**, 219906 (2006).
[32]A. Hellman, B. Razaznejad, and B. I. Lundqvist, "Potential-energy surfaces for excited states in extended systems," J. Chem. Phys. **120**, 4593–4602 (2004).
[33]R. J. Maurer and K. Reuter, "Excited-state potential-energy surfaces of metal-adsorbed organic molecules from linear expansion Δ-self-consistent field density-functional theory (ΔSCF-DFT)," J. Chem. Phys. **139**, 014708 (2013).
[34]X. Jiang, Z. Xu, Y. Zheng, J. Zeng, K.-Q. Chen, and Y. Feng, "Origin of broadband emission and large Stokes shift in antimony trisulfide," J. Phys. Chem. Lett. **13**, 8026–8032 (2022).
[35]G. L. W. Hart and R. W. Forcade, "Algorithm for generating derivative structures," Phys. Rev. B **77**, 224115 (2008).
[36]C.-C. He, J.-H. Liao, S.-B. Qiu, Y.-J. Zhao, and X.-B. Yang, "Biased screening for multi-component materials with Structures of Alloy Generation and Recognition (SAGAR)," Comput. Mater. Sci. **193**, 110386 (2021).
[37]S. B. Zhang, S.-H. Wei, and A. Zunger, "Stabilization of ternary compounds via ordered arrays of defect pairs," Phys. Rev. Lett. **78**, 4059–4062 (1997).
[38]L. D. Landau, *Statistical Physics* (Butterworth-Heinemann, 1980).
[39]S. Maintz, V. L. Deringer, A. L. Tchougréeff, and R. Dronskowski, "LOBSTER: A tool to extract chemical bonding from plane-wave based DFT," J. Comput. Chem. **37**, 1030–1035 (2016).
[40]R. Nelson, C. Ertural, J. George, V. L. Deringer, G. Hautier, and R. Dronskowski, "Lobster: Local orbital projections, atomic charges, and chemical-bonding analysis from projector-augmented-wave-based density-functional theory," J. Comput. Chem. **41**, 1931–1940 (2020).
[41]M. Yu and D. R. Trinkle, "Accurate and efficient algorithm for Bader charge integration," J. Chem. Phys. **134**, 064111 (2011).